



Delft University of Technology

Aeroelastic Wing Demonstrator with a Distributed and Decentralized Control Architecture

Mkhoyan, T.; Wang, Xuerui; De Breuker, R.

DOI

[10.2514/6.2022-1551](https://doi.org/10.2514/6.2022-1551)

Publication date

2022

Document Version

Final published version

Published in

AIAA SCITECH 2022 Forum

Citation (APA)

Mkhoyan, T., Wang, X., & De Breuker, R. (2022). Aeroelastic Wing Demonstrator with a Distributed and Decentralized Control Architecture. In *AIAA SCITECH 2022 Forum* Article AIAA 2022-1551 (AIAA Science and Technology Forum and Exposition, AIAA SciTech Forum 2022). <https://doi.org/10.2514/6.2022-1551>

Important note

To cite this publication, please use the final published version (if applicable). Please check the document version above.

Copyright

Other than for strictly personal use, it is not permitted to download, forward or distribute the text or part of it, without the consent of the author(s) and/or copyright holder(s), unless the work is under an open content license such as Creative Commons.

Takedown policy

Please contact us and provide details if you believe this document breaches copyrights. We will remove access to the work immediately and investigate your claim.



Aeroelastic Wing Demonstrator with a Distributed and Decentralized Control Architecture

Tigran Mkhoyan^{*}, Xuerui Wang[†], Roeland De Breuker[‡]
Delft University of Technology, Delft, The Netherlands

This study investigated the design and development of an autonomous aeroservoelastic wing concept with distributed flaps. This wing demonstrator was developed in the scope of the SmartX project, aiming to demonstrate in-flight performance optimization and multi-objective control with over-actuated wing designs. Following a successful test campaign with a previous wing design based on active morphing, this study aims to develop an over-actuated aeroelastic wing design suitable for aeroelastic control, including flutter suppression, maneuver and gust load alleviation. A decentralized control architecture is developed for the over-actuated and over-sensed system, allowing efficient sensing data processing and control algorithms. Aerodynamic and structural analyses are performed to determine actuator torque requirements and actuation mechanism design. Furthermore, buckling analysis is performed to size the wing structure. A state-space aeroelastic dynamic model is established to analyze the gust response and control effectiveness of the wing. It is established that a linear quadratic regulator significantly improves the closed-loop performance. Furthermore, the hypotheses are confirmed that fast actuation improves load alleviation performance and high-frequency disturbance rejection effectiveness. The manufacturing and integration of the wing demonstrator are discussed, which lay a foundation for future static and dynamic wind-tunnel experiments.

I. Introduction

The advancements in aircraft materials, manufacturing technology, control algorithms, and hardware design allow developing increasingly flexible aircraft concepts. Generally, flexibility comes as a side effect of lighter aircraft design and must be considered adequately. However, a more natural approach is to utilize the flexibility for the benefit of better performance, much like it is seen in nature with wing morphing for better gliding performance [1, 2]. As in nature, flexible wing concepts have been evolving since the early years of aviation. One of the well-documented examples was the active roll control of the Wright Flyer, the first successful heavier-than-air powered aircraft. In this lightweight design, the lateral stability was ensured by wing twist-warping [3]. This was possible because the flexible fabric-wrapped structure was well suited for morphing. As the flight speeds and loads were increased with the advancement of flight, a stiffer wing was required to fulfill structural requirements and overcome aeroelastic instabilities. As a result, the considerably more rigid wing design - generally optimized for cruise conditions - is faced with a compromised performance at other flight conditions. To harness the potential of a flexible wing, two design choices are possible: active morphing design and conventionally flapped distributed wing designs. Both design concepts can allow the lift distribution to be tailored actively, potentially reducing this performance loss and improving aircraft performance across the flight envelope. Furthermore, both design concepts can be distributed and modular (i.e., having multiple flaps along the span). They were mimicking the distributed nature of feathers found in avian biology.

While active morphing benefits aerodynamic efficiency, the morphing mechanism required for smooth shape control generally needs larger actuation forces and a more complex design. In our previous study, we have demonstrated a seamless morphing wing concept [4, 5], the SmartX-Alpha, capable of performing objectives such as shape control, drag minimization, and simultaneous gust and maneuver load alleviation [6]. This design showed a significant advantage over previous morphing concepts, allowing the lift distribution to be controlled locally by individually adjusting the camber and twist of each morphing module. However, the complexity of the morphing mechanism and increased

^{*}Ph.D. candidate, Faculty of Aerospace Engineering, Aerospace Structures and Materials department, T.Mkhoyan@tudelft.nl, P.O. Box 5058, 2600GB Delft, The Netherlands.

[†]Assistant Professor, Faculty of Aerospace Engineering, Department of Aerospace Structures and Materials & Department of Control and Operations, X.Wang-6@tudelft.nl, P.O. Box 5058, 2600GB Delft, The Netherlands, Member AIAA.

[‡]Associate Professor, Faculty of Aerospace Engineering, Aerospace Structures & Computational Mechanics, R.DeBreuker@tudelft.nl, P.O. Box 5058, 2600GB Delft, The Netherlands, Associate Fellow AIAA.

torque required for morphing require actuators with high continuous torque. The current study aims to address this gap and investigate the potential of *discrete morphing* with conventionally free hinged flaps. The benefit is significantly lower actuation forces and a simpler actuation mechanism. This initiated the development of the SmartX-Neo wing demonstrator concept. This paper describes the design and aeroelastic analysis of the wing demonstrator. Furthermore, the development and integration of the wing concept are discussed for future static and dynamic wind-tunnel experiments at the Open Jet Facility (OJF).

The main contribution of this paper is threefold. First, an aeroelastic wing demonstrator with distributed control surfaces is designed, analysed, and manufactured. Second, a distributed and decentralized control architecture is proposed and implemented. Third, dynamic closed-loop simulations of the demonstrator in the presence of gusts verified the structure and actuator design and highlighted the necessity of distributed control for local load alleviation.

The structure of the paper is as follows. The philosophy of SmartX is presented in Sec. II, followed by the design methodology in Sec. III. The demonstrator manufacturing and integration are presented in Sec. IV. The results are shown and discussed in Sec. V. Finally, conclusions are drawn in Sec. VI.

II. SmartX Philosophy

In the following sections, Sec. II.A and Sec. II.B, the aim of the SmartX project and the objectives of the SmartX-Neo are presented.

A. Goals of SmartX

The SmartX project aims to demonstrate in-flight performance optimization of several objectives such as (i) drag optimization, (ii) load alleviation, (iii) flutter suppression, and (iv) shape control through multidisciplinary integration of control sensing and morphing design. In the scope of this project, a smart morphing wing was developed: the SmartX-Alpha is capable of continuous active morphing with distributed Translation Induced Camber (TRIC) [7]. The advantage of this design was the capability of local control of the lift distribution along the span through individual adjustment of the camber and twist of each morphing module. This allows the wing to settle into the most optimal lift to drag ratio (*shape control*) to *minimize drag* and perform the *load alleviation* tasks [6].

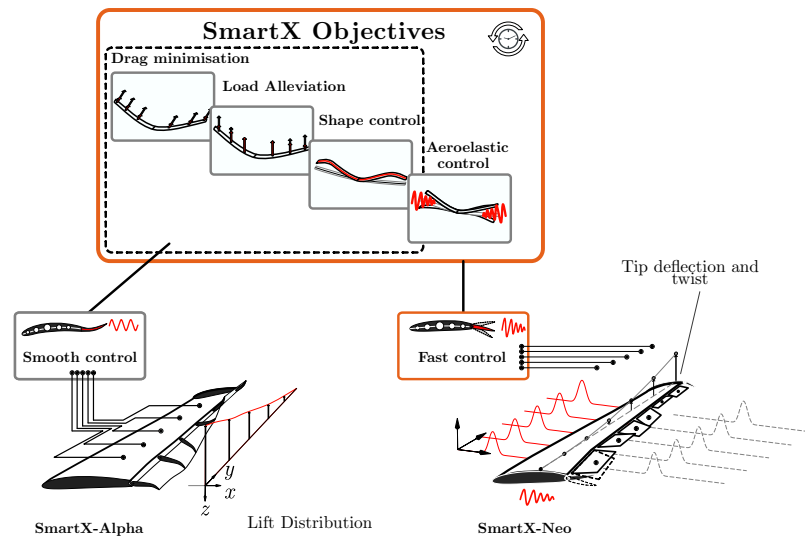


Fig. 1 Comparison of the objectives of the SmartX-Alpha and SmartX-Neo.

B. Objectives of SmartX-Neo

With this design, the first three objectives of the SmartX were achieved. However, due to limitations of the actuation bandwidth, faster objectives such as flutter suppression were not achievable with morphing alone. The bandwidth limitation arises due to two reasons. Firstly, due to the nature of the TRIC morphing concept, the morphing mechanism

of the SmartX-Alpha relies on a *loaded* hinge concept. The skin acts as a hinge between the rigid wing box and the flexible trailing edge, and this requires higher torque from the servo to overcome the internal strain. Higher torque servos generally have to compromise in actuation speed. The current study aims to address this gap and investigate the potential of *discrete morphing* with conventionally free hinged flaps. The benefit is significantly lower actuation forces and a simpler actuation mechanism. This yielded the concept of the SmartX-Neo* as shown in Fig. 1.

The SmartX-Neo was developed to investigate the following:

- comparison of *Discrete morphing* versus smooth morphing in terms of actuation bandwidth and design complexity;
- benefits of conventionally hinged flap versus morphing;
- benefits of over-actuated wing concept for aeroelastic control with advanced control methods;
- influences of the actuation speed on the control objectives.

III. Design Methodology

In the following sections, the design methodology of the SmartX-Neo is presented. Section III.A discusses the wing and aircraft planform design. The aeroservoelastic model and the control design are presented in Sec. III.B and Sec. III.C. The actuator model and the hypotheses of the numerical experiment are presented in Sec. III.D and Sec. III.E.

A. Planform Design and Analysis

The wing design was evaluated using an aerodynamic model, built with XFLR5 [8] and a Finite Element Model (FEM) built with ABAQUS [9], representing the structure of the wing.

1. Planform Design

The wing model was designed to investigate the benefits of advanced control methods for over-actuated aeroelastic wings and the aim to be integrated into an autonomous glider platform. The aim was to conduct a wind tunnel test in the Open Jet Facility (OJF) at the Delft University of Technology, equipped with a gust generator [10]. The wing design is evaluated for the condition of 35 m/s at a cruise angle of 4 degrees. The free stream velocity is chosen with a margin over the wind tunnel's maximum available free stream velocity. The cruise angle of attack is determined through preliminary design and assessment of the suitable flight platform and glider configuration. This is discussed in brief in the following sections.

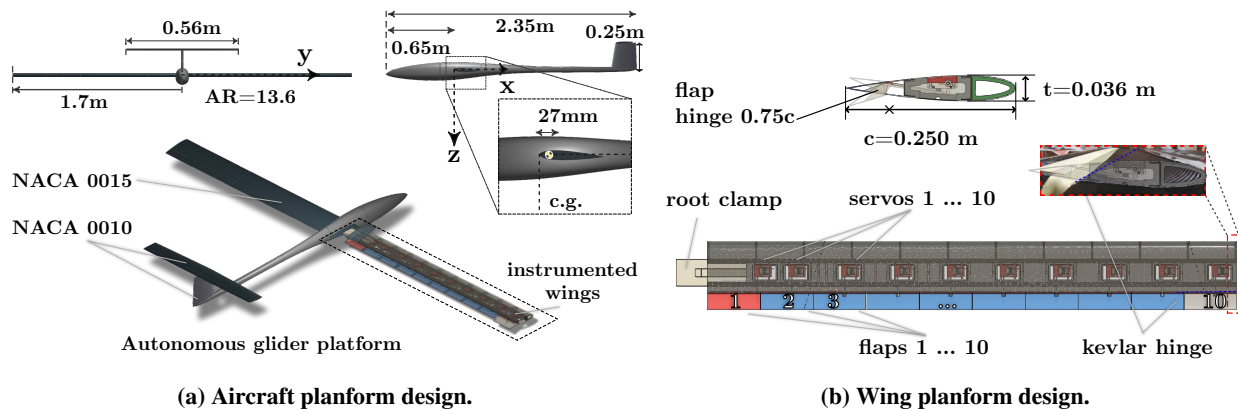


Fig. 2 Overview of the wing planform design.

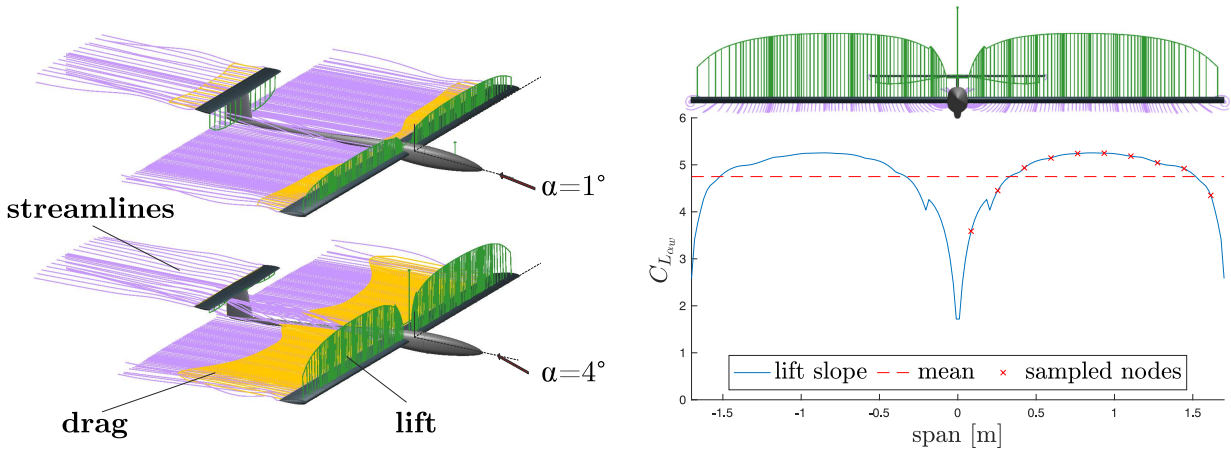
NACA0015 was selected as the wing profile as a good trade-off between aerodynamic performance and required structural components and instrumentation volume. The span was selected as 1.7 m considering the manufacturing constraint of the mold. The planform is shown in Fig. 2.

Preliminary design of the glider platform was conducted in XFLR5. A conventional aircraft configuration was chosen, with the elevator and vertical stabilizer conventionally actuated in a typical glider configuration. A thinner airfoil, NACA0010, was chosen for these wings as there was no requirement for large component volume compared to

*The project video can be found at <https://www.youtube.com/watch?v=WuxM2vmumkQ>

highly instrumented main wings. The elevator and vertical stabilizer were sized relative to the main wing according to common ratios, such that a balanced design was obtained. The relative placement of the wings and the body was achieved via steady-state stability analysis in XFLR5 at cruise conditions. With a total wing mass of 5.7 kg and payload mass of 1.5 kg, a center of gravity (COG) x location of 27 mm aft of the main wing leading edge was found, which provided sufficient lateral stability to trim the aircraft in cruise condition at $\alpha = 4^\circ$. The neutral point was found to be 0.305 m aft of the main wing. The remainder of the parameters are presented in Appendix A and Tab. 6.

2. Aerodynamic and Structural Design



(a) Aerodynamic analysis for conditions $\alpha = 4^\circ$ and $\alpha = 1^\circ$, at $V_\infty = 35$ m/s. (b) Lift slope $C_{L_{\alpha_w}}$ distribution main wing used in the aeroservoelastic model, $V_\infty = 35$ m/s, $\alpha = 4^\circ$.

Fig. 3 Aerodynamic analysis and win lift distribution.

To fulfill the requirements of the wind tunnel model, assess the aerodynamic load expected on the wing structure, as well as the lift generated by the flaps, an aerodynamic model was built using XFLR5. This software is based on the 2D analysis capabilities of XFOIL and implements the Vortex Lattice Method (VLM), and the 3D panel method [8, 11]. The resulting torque on the flap hinge was extracted from the aerodynamic analysis performed in XFLR5, allowing to evaluate of the lift generated by the flap and wing. The aerodynamic mesh was selected to have 2600 VLM panels and 5225 3D panels, with a 13 (cosine) \times 10 (sine) distribution along chord and span.

A type 1 (fixed speed) viscous analysis (Viscosity=1.5e-05 m²/s) was performed at $V_\infty = 35$ m/s, $\alpha = 4^\circ$ degrees of angle of attack to obtain lift distribution along the span of the wing planform at cruise condition. This is the distribution (blue curve) shown in 3b, the red curve is the mean distribution used as the wing lift coefficient $C_{L_{\alpha_w}}$. The top figure shows the streamlines (wake) in purple, generated behind the wing and near the wingtips at this condition. Fig. 3a shows the 3D lift distribution (green), induced drag (yellow) and streamlines (magenta) at $V_\infty = 35$ m/s and two angles of attack, $\alpha = 4^\circ$ and $\alpha = 1^\circ$. The latter angle is selected to show the configuration of the elevator. The figure shows that the elevator is designed with a fixed (4 degrees) negative incidence angle to balance the aircraft at level flight and compensate for the moment generated by the main wing. At cruise (bottom figure), the majority of lift is generated by the main wing.

3. Buckling Analysis

The wing-box structure was constructed to reinforce the structural design. Design iterations were evaluated in terms of buckling resistance. The worst-case condition ($V_\infty = 50$ m/s, $\alpha = 4^\circ$, $\delta_{\text{flap}} = 25^\circ$) were imposed on the structural FEM model in Abaqus to investigate the buckling behavior. This analysis was necessary due to the flexibility of the structure and the high number of cutouts made in the skin for actuator access bay panels. A limit load of 750 N was established. Figure 4a shows the setup of the Abaqus model. Two loads were applied, lift load F_y and torsional moment, M_x to make a conservative estimation of the aerodynamic loads induced during the worst-case condition. The boundary conditions (Bsc) were imposed to clamp the wing at the root.

Design iteration was made for a suitable rib design, and rib pitch and shape no buckling occurred below the maximum

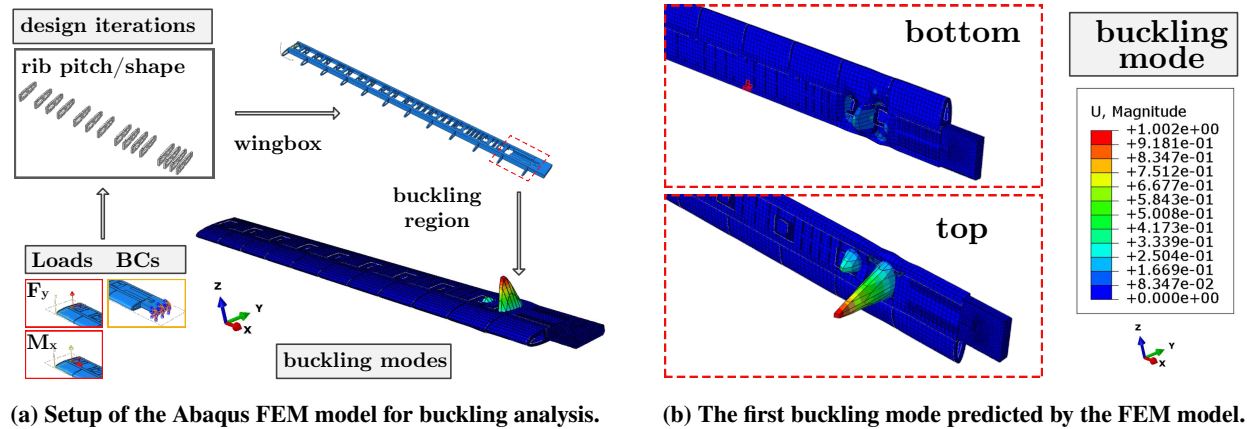


Fig. 4 Buckling model setup and analysis.

limits. After initial iterations, the weak point in the design was found to be near the buckling region, between the first cutout panel for servo 1 (Fig. 2a) and the wing clamp bonded at the root. Additional reinforcing ribs were added to support the cutout region, as shown in Fig. 5a. The result of the linear analysis for the first buckling mode with the final wing-box design is shown in Fig. 4b. The eigenvalue for the first mode was found at -1002.4 , well above the limit loads.

4. Actuator Selection

The actuation loads and the resulting flap moments were evaluated to determine the actuator's torque requirements in XFLR5 and select a suitable actuator. The analysis was conducted at 35 m/s. The angle of attack was maintained at $+4^\circ$. Fig. 6 shows a comparison of two servo configurations and the achievable control objectives for SmartX-Alpha versus SmartX-Neo. The right one shows the characteristics of the servo selected for the SmartX-Alpha demonstrated. Here, the actuator torque requirement was evaluated for various morphing conditions of the flaps [4].

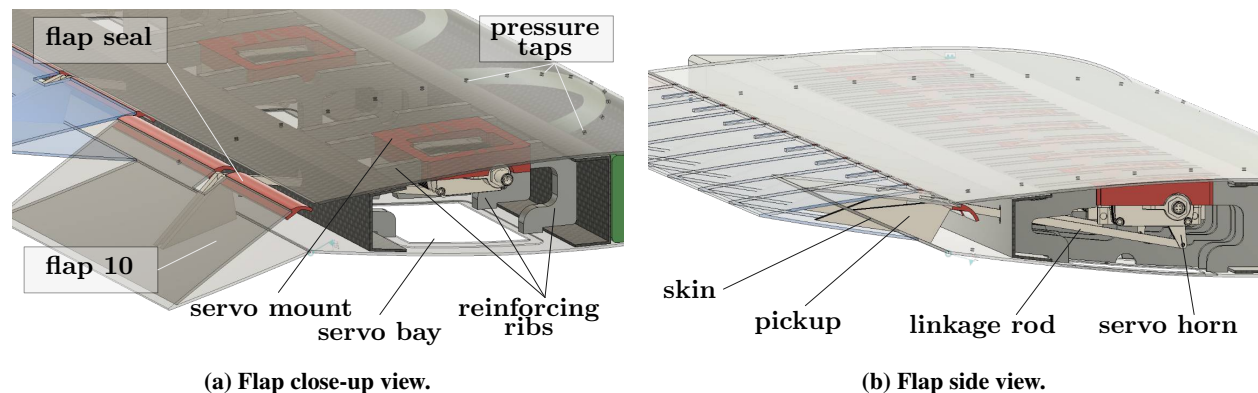
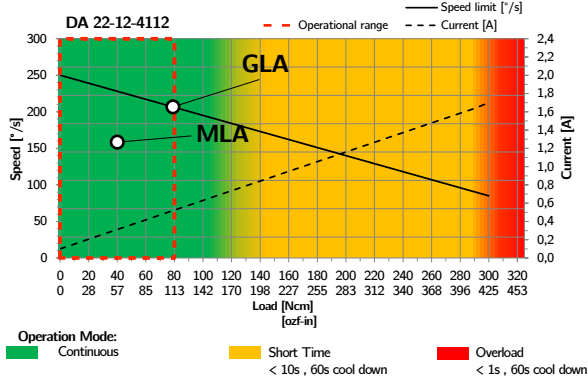


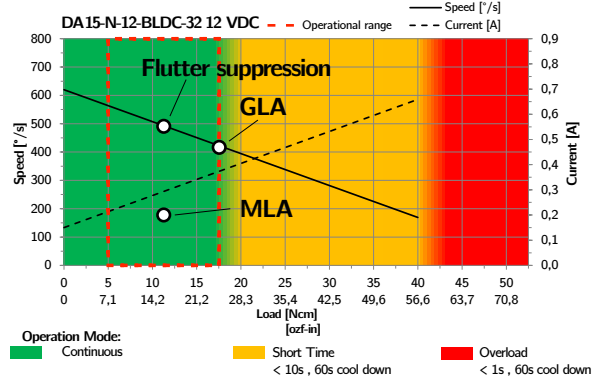
Fig. 5 Overview of the actuation mechanism.

As opposed to a simple flap design of the SmartX-Neo (Fig. 5a), the morphing mechanism of the SmartX-Alpha required relatively high torque servos, which are limited in continuous actuation speed (Fig. 6a). In turn, the ability to fulfill the control objectives is limited as well. In contrast, the faster servo depicted on the right (Fig. 6b) shows higher continuous actuation capability and wider scope of possible control objectives. The white dots indicated in Fig. 6 are potential operational points described in Fig. 1. Gust Load Alleviation (GLA) can be maximized at the highest torque and continuous load setting. Maneuver Load Alleviation (MLA) is less limiting on actuation speed, as this objective can be achieved in a longer time scale.

The aerodynamics analysis performed for the SmartX-Neo yielded three times faster continuous actuation and six times lower loads on the control surface (10 Nm versus 60-80 Nm) for SmartX-Neo compared to SmartX-Alpha [4]. The actuator continuous actuator bandwidth of the selected servo is presented in Fig. 6b. The Volz DA-15-N-BLDC servo was



(a) Volz DA-22-12-4112 performance parameters [12] and the SmartX-Alpha requirements.



(b) Volz DA-15-N-BLDC performance parameters [12] and the SmartX-Neo requirements.

Fig. 6 Comparison of the actuator continuous torque requirement, SmartX-Alpha versus SmartX-Neo.

selected due to its high continuous load and position feedback capabilities. Figure 6b shows the performance specification data of the actuator published by the manufacturer [12] and the comparison between the Volz DA-22-12-4112 used for the SmartX-Alpha. The green region indicates the range in which the servo can operate continuously. As seen, the peak torque requirement, indicated with a red-dotted box, falls within the continuous operation range of the servo.

B. Aeroservoelastic Model

An aeroservoelastic model is developed in Matlab/Simulink to access actuator requirements concerning the expected dynamic response of the wing demonstrator and develop a controller capable of fulfilling the objectives of the SmartX-Neo. The model is adapted from [13] and represents a coupled unsteady aeroservoelastic model, trimmed at an air density $\rho_{\text{air}} = 1.225 \text{ kg/m}^3$ and free stream velocity $V_{\infty} = 35 \text{ m/s}$. It is composed of ten aerodynamics strips placed at equal distances and the span corresponding to the number of flaps.

1. Structure

The structure is modeled as a linear Euler-Bernoulli beam. Each actuator (flap) is modeled as a second-order mass-spring-damping system, with a hinge moment control input M_f^{act} . The clamped beam-flap model four degrees of freedom at each node, represented by the state vector $\mathbf{x}_s = [w \ \phi \ \theta \ \beta]^T$. Where, w , ϕ , θ , represent the transverse displacement ($\downarrow +$), bending ($\cup +$), torsion ($\cup +$) and β is the flap rotation angle ($\cup +$). The dynamics for the clamped beam are given by:

$$\mathbf{M}_s \ddot{\mathbf{x}}_s + \mathbf{C}_s \dot{\mathbf{x}}_s + \mathbf{K}_s \mathbf{x}_s = [\mathbf{F}_r \ \mathbf{F}_{\text{ext}}] \quad (1)$$

Where \mathbf{M}_s , \mathbf{C}_s , \mathbf{K}_s and structural mass damping and stiffness matrices, respectively. On the right-hand side, \mathbf{F}_r and \mathbf{F}_{ext} are the wing root reaction forces and the distributed external forces. The wing root reaction forces are, shear force, the root bending moment, and torsion moment contained in vector $\mathbf{F}_r = [F_w \ M_\phi \ M_\theta]^T$. Structural damping is added proportionally to the stiffness matrix, though $\mathbf{C}_s = k \mathbf{K}_s$, where \mathbf{C}_s is the damping matrix and k_s a scaling factor.

In Eq. (1) beam structural mass and stiffness matrices \mathbf{M}_s and \mathbf{K}_s are augmented to include the effect of the flap, yielding $\mathbf{M}_s^{\text{aug}}$ and $\mathbf{K}_s^{\text{aug}}$, as follows:

$$\mathbf{M}_s^{\text{aug}} = \begin{bmatrix} \mathbf{M}_s & \begin{matrix} S_\beta \\ 0 \\ I_\beta + b(c-a)S_\beta \\ I_\beta \end{matrix} \\ \begin{matrix} S_\beta \\ 0 \\ I_\beta + b(c-a)S_\beta \end{matrix} & \begin{matrix} S_\beta \\ 0 \\ I_\beta \end{matrix} \end{bmatrix}, \quad \mathbf{K}_s^{\text{aug}} = \begin{bmatrix} \mathbf{K}_s & \begin{matrix} 0 \\ 0 \\ 0 \\ K_\beta \end{matrix} \\ \begin{matrix} 0 \\ 0 \\ 0 \end{matrix} & \begin{matrix} 0 \\ 0 \\ 0 \\ K_\beta \end{matrix} \end{bmatrix} \quad (2)$$

In Eq. (2), the flap angle state β is coupled with the main beam structure through inertia couplings and a rotational spring, serving as actuator stiffness. The measurable outputs are the shear force, the root bending moment, and the node displacements in the heave direction w . In total, ten nodes are movable; the first node denotes as 0^{th} , is the reference node at the root (clamped). The remaining nodes are labeled 1-10th and correspond to the center location of each flap as shown in Fig. 7.

In total, ten nodes are movable; the first node denoted as 0^{th} , is the reference node at the root (clamped). The remaining nodes are labeled 1-10th and correspond to the center location of each flap as shown in Fig. 7.

2. Aerodynamics

Because of the high aspect ratio of the wing, the two-dimensional strip theory was adopted where the unsteady aerodynamic forces on each strip are represented in a time-domain formulation, equivalent to Theodorsen's frequency-domain model [14]. The time-domain formulation used in this study is the indicial function approximation by Leishman [15].

Referring to Ref. [15] four lag states are introduced for each aerodynamic strip to model the circulatory part of the aerodynamic response. Similar to the structural part, aerodynamic state vector is represented by $\mathbf{x}_a = [w \ \phi \ \theta \ \beta \ z_i]^T$. Where the latter entry are the lag states. The aerodynamic force vector, \mathbf{F}_a , is defined as:

$$\mathbf{F}_a = \mathbf{M}_a \ddot{\mathbf{x}}_a + \mathbf{C}_a \dot{\mathbf{x}}_a + \mathbf{K}_a \mathbf{x}_a + \mathbf{K}_z z_i \quad (3)$$

3. Couplings

The coupling of the structural and the aerodynamic models is described in [13]. The full aeroservoelastic model contains the following states:

$$\mathbf{x}_{ae} = [\dot{\mathbf{x}}_s \ \mathbf{x}_s \ z_1 \ z_2 \ z_3 \ z_4]^T \quad (4)$$

where \mathbf{x}_s is the structural state vector, representing the nodal degrees-of-freedom for each of the 11 nodes; z_1, z_2, z_3, z_4 are the aerodynamic lag states.

An overview of the coordinate system, nodes and axis definitions of the aeroelastic system is presented in Fig. 7. Here O_w represents the right wing frame.

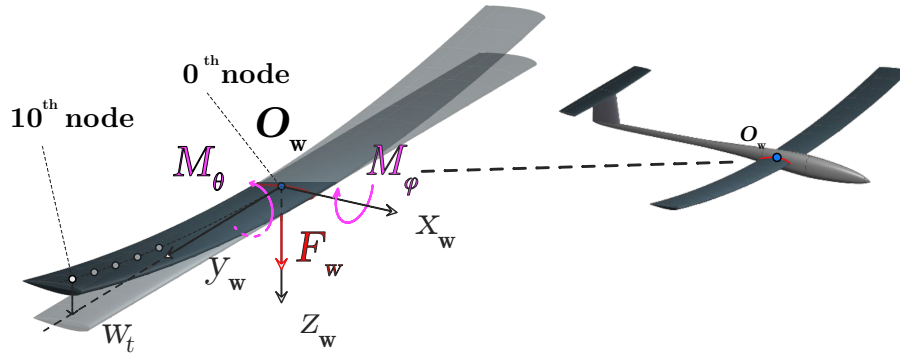


Fig. 7 Reference frames, axis definitions, and degrees of freedom of the aeroelastic system (the right wing).

4. Gust model

Initial assessment of the dynamic response is performed with a simplified gust model, a “1-cosine” gust profile, assumed to be uniform across the span and represented as an increment in α :

$$\alpha_g(t) = W_g (1 - \cos(\omega_g t)) \quad (5)$$

where W_g is the gust magnitude, and ω_g is the gust frequency in radians, calculated as $\omega_g = 2\pi f_g$. Here, f_g is the gust frequency in Hz.

C. Control design

The aeroservoelastic SmartX-Neo wing is controlled by a linear-quadratic regulator (LQR) controller [16]. This is a linear optimal control method that provides the optimal feedback gain matrix \mathbf{K} to stabilize the system. The aeroservoelastic wing is modelled in a state-space form as:

$$\dot{\mathbf{x}} = \mathbf{A}\mathbf{x} + \mathbf{B}\mathbf{u} + \mathbf{B}_g\alpha_g \quad (6)$$

$$\mathbf{y} = \mathbf{C}\mathbf{x} + \mathbf{D}\mathbf{u} \quad (7)$$

Where \mathbf{A} , \mathbf{B} , \mathbf{B}_g , \mathbf{C} , \mathbf{D} are the system dynamic matrices, while the gust angle of attack input α_g is defined in Eq. (5).

The gain matrix is obtained to minimize the objectives of interest, namely: the wing root shear force F_w , the wing root bending moment M_ϕ , and the wing tip displacement w_t . The state feedback law minimizes the quadratic cost function [17]:

$$J = \int_0^\infty [\mathbf{x}^\top \mathbf{Q}\mathbf{x} + \mathbf{u}^\top \mathbf{R}\mathbf{u}] dt \quad (8)$$

where the weight matrices \mathbf{Q} and \mathbf{R} are positive definite matrices that penalize the cost of deviation of the states from zero and the cost of actuation, respectively. The state feedback gain matrix that minimizes the cost is defined by $\mathbf{K} = \mathbf{R}^{-1}\mathbf{B}^\top \mathbf{S}$, where \mathbf{S} is the solution to the Riccati equation:

$$\mathbf{A}^\top \mathbf{S} + \mathbf{S}\mathbf{A} - \mathbf{S}\mathbf{B}\mathbf{R}^{-1}\mathbf{B}^\top \mathbf{S} + \mathbf{Q} = \mathbf{0} \quad (9)$$

The closed-loop system dynamics are:

$$\dot{\mathbf{x}} = \mathbf{A}\mathbf{x} + \mathbf{B}\mathbf{u} + \mathbf{B}_g\alpha_g = \underbrace{(\mathbf{A} - \mathbf{B}\mathbf{K})}_{\mathbf{A}_{clp}} \mathbf{x} + \mathbf{B}_g\alpha_g \quad (10)$$

In this paper, \mathbf{Q} is chosen as $\mathbf{C}^\top \mathbf{C}$, while \mathbf{R} is chosen as an identity matrix \mathbf{I}_n , with $n = 10$. It is noteworthy that the gust is unknown to the controller. The LQR assumes that full state feedback is available. Suppose full state feedback is not available for a real-life system. In that case, the Linear Quadratic Gaussian (LQG) control law can be designed, which contains a Kalman filter state estimations using a combination of sensory measurements (e.g., cameras, gyros).

D. Actuator dynamics

One of the objectives of this study is to investigate how design changes in actuation can affect the performance of control objectives (Fig. 1). In particular, the study aims to assess the role of faster actuation for achieving these control objectives. It is to be expected that the servo bandwidth influences the performance of gust load alleviation. Therefore, a parametric model of actuator dynamics is constructed to investigate its influence. Actuator dynamics can be modeled by a second-order system, which is analogous to a mass-spring-damping system. To parametrically adjust the damping and stiffness parameters, a parameter k is chosen, with the following relationship:

$$\mathbf{K}_\beta = \mathbf{K}_f k^2, \quad \mathbf{C}_\beta = \mathbf{C}_f k \quad (11)$$

where \mathbf{K}_β and \mathbf{C}_β are the stiffness and damping matrices in the augmented structural model corresponding to the entries of the flap. The matrices \mathbf{K}_f and \mathbf{C}_f are the original actuator stiffness and damping matrices. Equation (11) ensures that the natural frequency of the actuator dynamics is scaled proportionally, while the damping ratio is kept invariant.

E. Hypotheses

The analysis performed in this study shall be limited to Gust Load Alleviation (GLA) and the influence of actuator dynamics. Considering these constraints and the assumptions made in the aeroservoelastic model and the actuator model, two hypotheses are formulated:

- 1) the first hypothesis is that higher actuator bandwidth will be more effective for gust load alleviation;
- 2) the second hypothesis is that a higher actuator shall allow more effective GLA at higher gust frequencies.

The last hypothesis means that we expect that faster actuators will allow the controller to respond faster to more high-frequency disturbances encountered by the system. In Sec. V simulations are set up to investigate the hypotheses.

IV. Demonstrator Manufacturing and Integration

The design analysis was utilized to manufacture a composite wing demonstrator, SmartX-Neo, with a wing-box structure and an integrated actuation mechanism.

A. Manufacturing Process

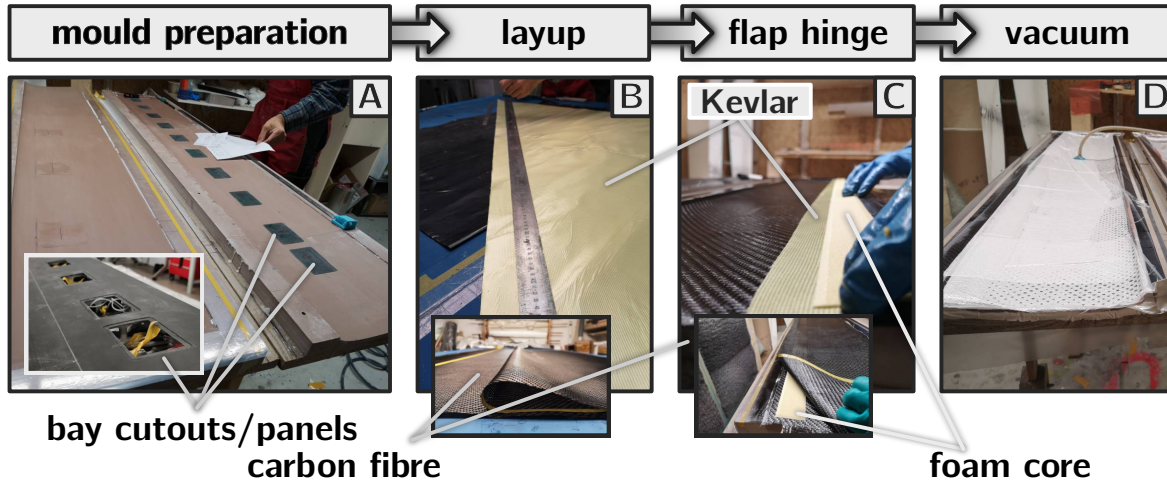


Fig. 8 Manufacturing process.

The composite wing design was constructed in four parts (i) top skin, (ii) bottom skin, (iii) wing box structure, and (iv) distributed flap modules. A mold consisting of top and bottom halves was manufactured out of Polyurethane based SikaBlock with a density of 650 kg/m^3 [18]. The composite wing skin consisted of three layers of 160 g/m^2 carbon fiber and additional fiberglass of 40 g/m^2 for a smooth surface finish. The skin was manufactured and cured with hand layup technique in the top and bottom vacuum bagged molds as shown in Fig. 8. The spars were cured in a separate mold and made of 2 layers of 160 g/m^2 carbon fiber and assembled in the main wing structure.

Figure 8 shows the first phase of the manufacturing process in sub-figures A-D. This process is initiated by the preparation of the mold (Fig. 8-A), where the pre-manufactured servo panels covers are arranged at the location of the cutouts. The panels are placed underneath the initial layer such that the actual panel cutouts are formed to the specifications, and the surface is smooth. Ten cutouts were made to facilitate actuator maintenance and assembly, corresponding to 10 flaps per wing. The flaps are numbered as 1-10, with the 10 th flap corresponding to the outermost flap of module 10 and the 1 th flap the one closest to the fuselage, as indicated by the red color in Fig. 2a. Process A is followed by hand layup (Fig. 8-B), where the flap hinge material is stacked between the carbon fiber layers.

The hinge for the flap mechanism was based on foam-reinforced Kevlar material. A single strip of 110 g/m^2 Kevlar was added between carbon fiber layers 2 and 3 (most inner layer). Additionally, a Herex foam strip was added for additional stiffness as depicted in Fig. 8-C. The process is completed by vacuum bagging and curing (Fig. 8-D).

B. Integration Process

The assembly and integration process is depicted in sub-figures A-D of Fig. 9. The actuation mechanism was designed such that it was fully integrated inside the wing and could be assembled after the joining top and bottom parts (Fig. 9-A). The parts were 3D printed from polylactic acid (PLA) and used in the assembly process as shown in Fig. 9-B. A 3D-printed base was designed to house the actuators and bonded to the top skin, shown in the bottom part of sub-figure Fig. 9-A. To resist buckling, a supporting rib structure was added near the cutouts and bonded to the skin. The assembly process is shown in Fig. 9-C. Here, two wing halves were joined after the wiring and all assembly components were in place. To bond the two wing halves, epoxy was deposited on the contact surfaces between the wing-box. Epoxy-infused foam cores were arranged along the wing seams to ensure a stronger bond. The final step in the integration was the curing and demolding (Fig. 9-D).

The sensor and module integration process is depicted in sub-figures A-D of Fig. 10. An overview of the various

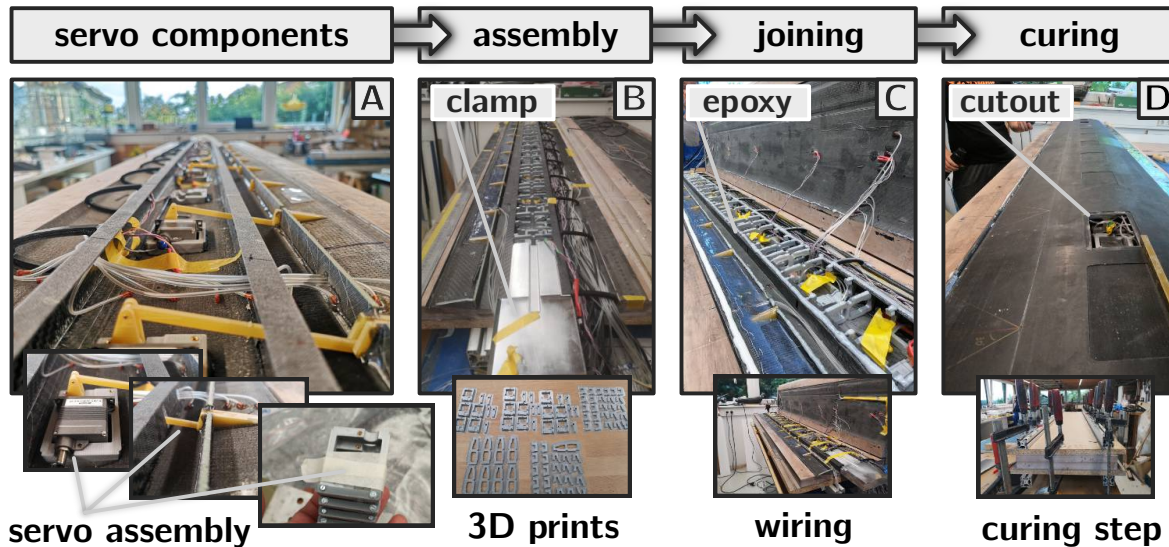


Fig. 9 Assembly integration process.

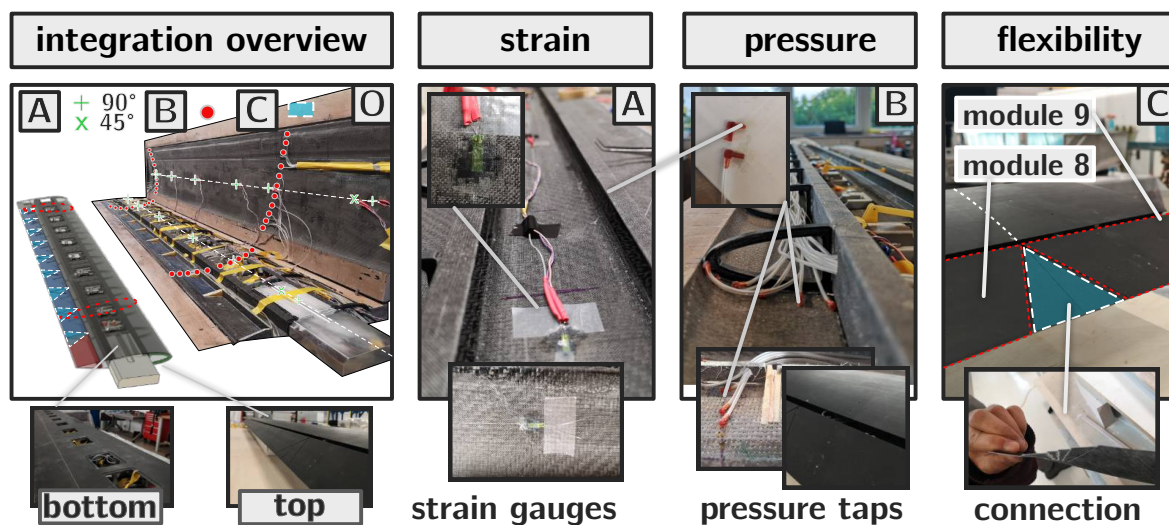


Fig. 10 Module and sensor integration.

sensors and their arrangement in the wing is shown in Fig. 10-A. Strain gauges (Fig. 10-B) were installed on top and bottom in 90° arrangement (shown as a plus) and 45° arrangement to measure the twist near the root (shown as a cross). In addition to the strain gauges, two fiber optics sensors were installed along the span on the top and bottom sides. Furthermore, pressure taps were installed (Fig. 10-C) to allow characterization of the pressure distribution in the wind tunnel test. These were arranged in an array of 22-28 taps per airfoil cross-section at approximately 15° angle with respect to the free stream velocity. This was done such that the interference in pressure measurements along the cord-wise taps was reduced. The tubing was guided through the wing root and D-box area at the root of the wing.

Flexible feather-like patches were integrated between the modules for improved the smoothness and the aerodynamic properties of the flaps. Fig. 10-D shows the triangular segment between the outer flap (9) and the adjacent flap (8). The segments were made of the same material as the skin, supported by elastomeric filler material. This filler material (Elastosil E41) was deposited during the integration phase from the inner side of the flap. Triangular cutouts were then made to facilitate flexibility.

A. Gust Load Alleviation

A state-space aeroelastic dynamic model was established to analyze the gust response and control effectiveness of the wing. The aeroelastic model as described in section III.B was subjected to discrete gust signals. The actuator dynamics implemented in the aeroservoelastic model were modified through the scaling parameter k governing the actuation design and dynamics (Sec. III.D).

1. Simulation Set-Up

Table 1 Simulation and design configurations.

	Design		Simulation		
	k [-]	f_g [Hz]	W_g [rad]	dt [s]	t_{sim} [s]
	1.00	1.00	$2/V_\infty$	0.001	1.20
input	0.75	2.00	$2/V_\infty$	0.001	1.00
	0.50	3.00	$2/V_\infty$	0.001	1.00

Three scaling values were chosen; additionally, three different gust frequencies were evaluated to assess the effectiveness of the controller, resulting in a total of 9 different simulation conditions. In each simulation, the control gain matrix was kept constant as described in Sec. III.C and an actuation limit of 25 degrees of flap deflection is considered. The simulation was evaluated at $\rho_{air} = 1.225 \text{ kg/m}^3$ and $V_\infty = 35 \text{ m/s}$. For slower gust ($f_g = 1 \text{ Hz}$), a longer simulation time was used to ensure the entire gust onset was captured. The varied input conditions are presented in Tab. 1. Each row of the design parameter k was varied with the entries of the simulation parameters (f_g, W_g, dt, t_{sim}). The first simulation run would thus consist of the first row of the table, and the second would be composed of parameters pairs: $k = 0.75, f_g = 1 \text{ Hz}, W_g = 2/35 \text{ rad}, dt = 0.001 \text{ s}, t_{sim} = 1.20 \text{ s}$. The parameters of the aeroservoelastic model, which were kept invariant, are presented in 2.

Table 2 Parameters of aeroservoelastic model.

Item	Symbol	Value	Unit
Half span	L_w	1.70	[m]
Chord	$2b$	0.25	[m]
Shear centre location	a	0.00	[m]
Wing lift coefficient	$C_{L_{\alpha_w}}$	4.75	[-]
Mass per unit length	m	0.75	[kg/m]
Flap mass per unit length	m_f	0.25	[kg/m]
Moment of inertia	I_θ	0.24	[kgm ²]
Bending stiffness	EI	$1/2 \cdot 10^3$	[Nm ²]
Torsional stiffness	GJ	10^5	[Nm]

In Eq. (11), $\mathbf{K}_f = 100$ and $\mathbf{C}_f = 10^{-4}$. To evaluate the performance of the closed-loop system, two metrics are used: the maximum percentage difference of the peak f_{max} and the area difference f_{area} between closed- and open-loop responses. For example, for the shear force F_w , the performance metric is defined as:

$$f_{max}(\Delta F_w) = \left(1 - \frac{\max(|F_w|)_{closed}}{\max(|F_w|)_{open}} \right) \cdot 100\% \quad (12)$$

The area difference defined for the shear force F_w is defined as:

$$f_{area}(\Delta F_w) = \left(1 - \frac{\text{area}(|F_w|)_{closed}}{\text{area}(|F_w|)_{open}} \right) \cdot 100\% \quad (13)$$

In Tables 3 and 4 the operator $f(\cdot)$ is used to describe the operation needed to obtain the aforementioned metrics.

2. Effects of Gust Frequency

The effectiveness of the controller for gust load reduction was evaluated for various gust inputs with parameters described in Tab. 1. The result of simulations for the metrics peak magnitude and peak area are presented Tab. 3 and Tab. 4, respectively. Herein, the values indicated are the percentage reduction of the specified metric as compared to the open-loop. Three gust load reduction objectives were considered, the shear force F_w , root bending moment M_ϕ , and the tip displacement w_t . The rows in the table indicate variations in the scaling parameter k .

Table 3 Gust load reduction comparison for metric peak magnitude for varying gust frequency and scaling.

Variables	$f_g = 1.00$ [Hz]			$f_g = 3.00$ [Hz]			$f_g = 5.00$ [Hz]		
	$f(\Delta F_{w_s})$	$f(\Delta M_{\phi_s})$	$f(\Delta w_{t_s})$	$f(\Delta F_{w_s})$	$f(\Delta M_{\phi_s})$	$f(\Delta w_{t_s})$	$f(\Delta F_{w_s})$	$f(\Delta M_{\phi_s})$	$f(\Delta w_{t_s})$
k=1.00	71.26	78.25	65.00	69.67	76.26	63.25	67.39	73.20	60.71
k=0.75	77.15	82.88	70.22	75.71	81.30	68.58	73.50	78.54	65.99
k=0.50	82.30	83.84	69.24	81.14	82.46	67.83	79.23	79.85	65.06
k=0.75 [$\Delta_{k=1}$]	+5.89	+4.63	+5.22	+6.04	+5.03	+5.33	+6.11	+5.34	+5.29
k=0.50 [$\Delta_{k=1}$]	+11.04	+5.59	+4.24	+11.47	+6.19	+4.58	+11.83	+6.65	+4.35

Looking at the first row, corresponding to the nominal actuator dynamics ($k = 1$), it is observed that significant reductions (65-85 %) are achieved for all metrics and objectives with the closed-loop control. Furthermore, it is observed that the reduction is consistently less effective for increasing gust frequencies (e.g., 71.78 %, 69.67 %, 67.39 % for shear force) for all objectives for the metric peak magnitude. This is consistent with the expectation that the higher gust frequency will induce a sharper disturbance onset from the wing in the open-loop, requiring faster effort by the controller (faster response). The time responses to the gust onset are plotted for the three objectives and the highest and lowest gust frequency in Figures 12 and 13, respectively. The gust input also follows a similar shape to the open-loop response, indicated by the blue dashed curve. The columns in these plots correspond to shear force, bending moment, and tip deflection, respectively. Here, it is observed that the peak magnitude for the open-loop is smaller for slower gusts. Besides, the response is also narrower. The effectiveness of GLA is determined by the ability of the controller to flatten the onset peak and reduce the area underneath the curve. The closed-loop responses at varying scales clearly support the effectiveness (e.g., ≈ 180 N versus ≈ 40 N for the shear force at 1 Hz).

3. Flap Deflections

Given that the amount of disturbance the controller can resist is constrained by the bandwidth of the actuator - in this model governed by a second-order system actuator dynamics - the effectiveness decreases as gust frequency increases.

The flap allocation corresponding to the gust onset and responses in Figures 12 and 13 are plotted in Figures 15a and 15b, where the flap location corresponds to the flap distribution along the span of the wing are differentiated by color. The shape of the line differentiates the varying scaling, dash-dotted, corresponding to the fastest actuator. The distributions observed for one and 5 Hz gusts, respectively, show significantly narrower flap onset and more actuator input to counter the gust (e.g., $\approx 15^\circ$ versus $\approx 25^\circ$) for inboard flaps. Furthermore, observing the differences between the nominal and fastest actuator (dash-dotted line), the flap angles are twice as high at $k=0.50$ (e.g., $\approx 10^\circ$ versus $\approx 20^\circ$ for flap four at 1 Hz).

4. Effect of Faster Actuator Dynamics

Consequently, as the bandwidth of the actuator is increased, the controller can react to the gust disturbance, and therefore the effectiveness of the GLA reduction should increase. Higher reduction percentages observed for lower scaling parameters, corresponding to rows in the mentioned Tables 3 and 4 confirm this hypothesis. The fourth and fifth rows in these tables represent the percentage difference of reduction compared to slower nominal dynamics; +, indicating improved delta. Here we see significant improvements in the GLA for all objectives. In particular, we see significant improvements in shear force and bending moment reduction (e.g., 5.89 %, 11.04 % for the shear force at 1 Hz) for increasing k .

A second critical observation can be made from the comparison of the deltas for each objective across varying frequencies. It is clear that the faster actuator positively impacts the controller effectiveness (e.g., 11.04%, 11.47%, 11.83%

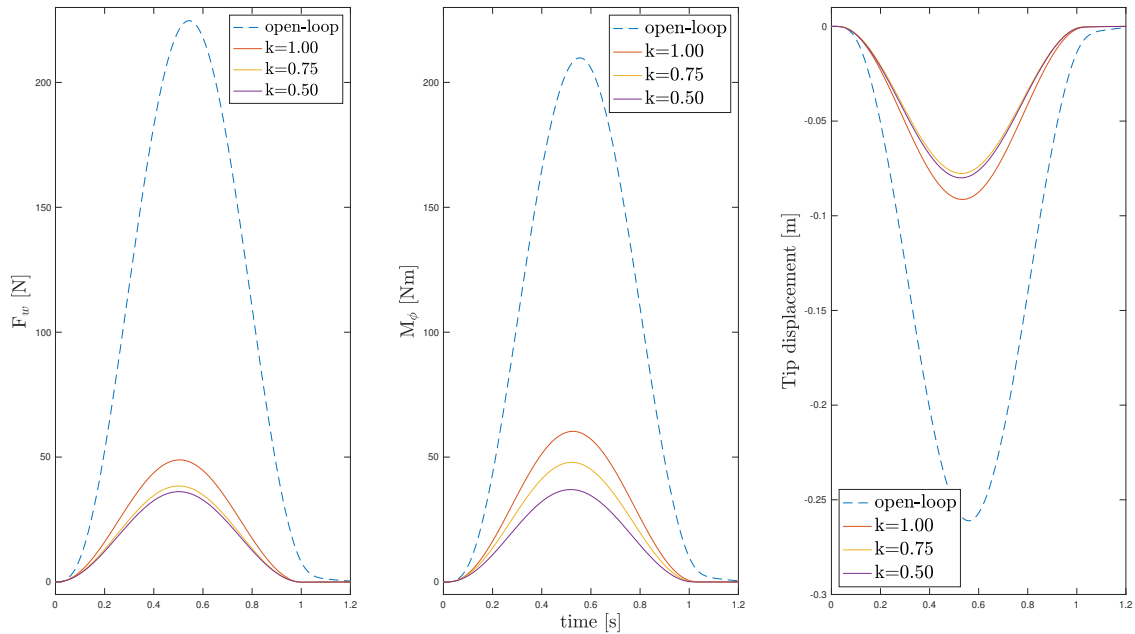


Fig. 12 Open and closed-loop wing response comparisons at gust frequency 1 Hz.

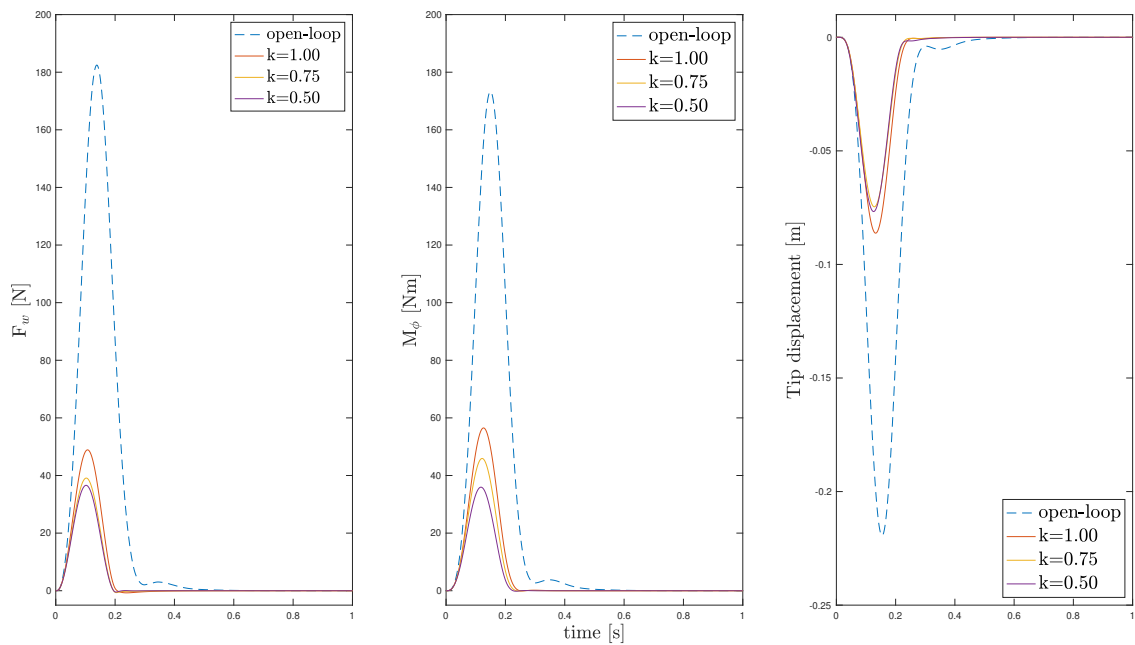


Fig. 13 Open and closed-loop wing response comparisons at gust frequency 5 Hz.

for the shear force at $k=0.50$ [$\Delta_{k=1}$] for faster gust onsets, confirming the second hypothesis, namely, that disturbance rejection for higher actuator bandwidth will be more apparent at higher gust frequencies. Differences are also observed across the objectives. Bending moment and tip displacement deltas follow the same trend, meaning better reduction for faster actuator but lower magnitude. The only exception to this lower positive delta reduction for $k=0.75$ compared to $k=0.5$ (e.g., 5.89 %, 11.04 % at 1 Hz) for the tip displacement. However, the faster actuator is still beneficial at higher gust frequencies even for this objective (e.g., +5.22 %, 5.33 %, 5.29 % $k=0.50$ [$\Delta_{k=1}$]). A possible explanation for the

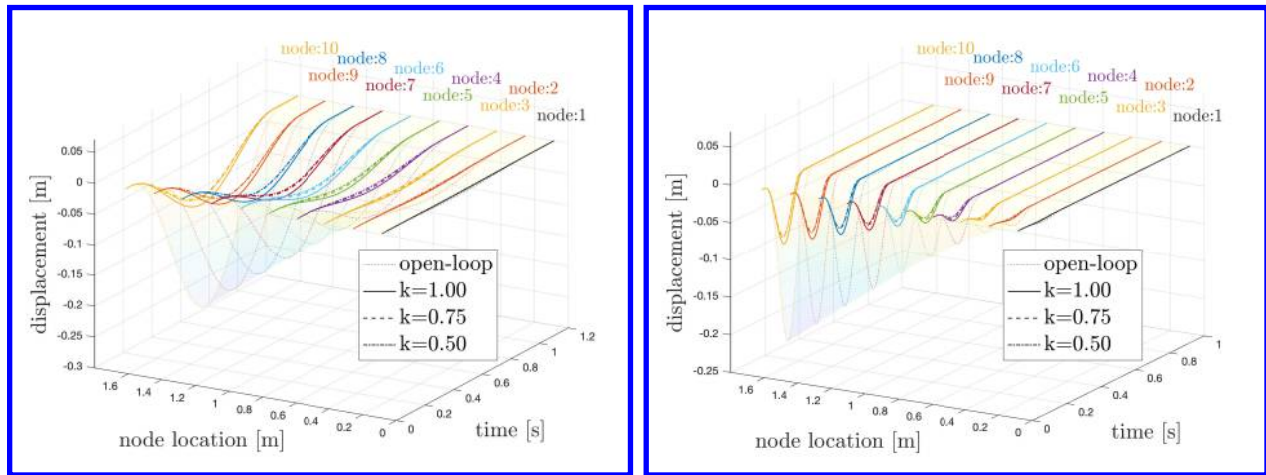
differences observed between the objectives is the time scale that characterizes their responses. The shear forces directly relate to instantaneous acceleration triggered by a gust event, being the faster the one, and thus more apparent to reduce. Similar observations are made from the time responses for closed-loop at different scaling parameters (Figures 12 and 13). Here, the curves corresponding to decreasing scaling parameter k are indicated by red, yellow, and magenta curves. In all cases, the magenta curve (the fastest actuator) is the flattest curve except for the tip displacement.

5. Differences in Metrics and Distributions

Table 4 Gust load reduction comparison for metric area for varying gust frequency and scaling.

Variables	$f_g = 1.00$ [Hz]			$f_g = 3.00$ [Hz]			$f_g = 5.00$ [Hz]		
	$f(\Delta F_{w_s})$	$f(\Delta M_{\phi_s})$	$f(\Delta w_{t_s})$	$f(\Delta F_{w_s})$	$f(\Delta M_{\phi_s})$	$f(\Delta w_{t_s})$	$f(\Delta F_{w_s})$	$f(\Delta M_{\phi_s})$	$f(\Delta w_{t_s})$
$k=1.00$ [-]	71.68	78.70	65.48	71.69	78.70	65.50	71.69	78.70	65.50
$k=0.75$ [-]	77.51	83.20	70.65	77.51	83.21	70.66	77.51	83.21	70.66
$k=0.50$ [-]	82.58	84.11	69.59	82.58	84.12	69.60	82.58	84.12	69.60
$k=0.75$ [$\Delta_{k=1}$]	+5.83	+4.51	+5.17	+5.82	+4.51	+5.17	+5.82	+4.51	+5.16
$k=0.50$ [$\Delta_{k=1}$]	+10.90	+5.42	+4.11	+10.89	+5.42	+4.11	+10.89	+5.42	+4.11

In Tab. 4 the result is shown for the metric area. Whereas the max peak metric shown in Tab. 3 is related to onset maxima and minima, the area metric is related to the shape of the response (area under the curve comparison) as shown in responses Figs. 12 and 13. Observing the shape of the curve between gust frequencies 1 and 5 Hz, it is seen that the gust onset the open-loop versus closed-loop scale consistently. This can explain why the area metric seems invariant to the gust frequency (e.g., the variations of the percentage differences are similar across gust frequencies). Observing the deltas in rows 4 and 5, we see a similar trend between the objectives (higher shear force reduction) and higher effectiveness for a faster actuator. It can also be concluded from these observations that, in general, the gust onset reduction mechanism of the LQR is aimed at reducing the area underneath the peak compared to the open-loop. The LQR controller archives this consistently for various gust frequencies. It is noteworthy that the LQR controller was kept invariant in these simulation scenarios.



(a) Wing node displacements 1 Hz. (b) Wing node displacements 5 Hz.
Fig. 14 Spanwise wing node displacements comparison for two frequencies and varying scaling parameter.

B. Initial Design Evaluation

Preliminary evaluation of the wing and planform design was performed based on the numerical simulations described in the previous section. The control allocation, particularly the maximum flap angles at the peak of the onset dictated by

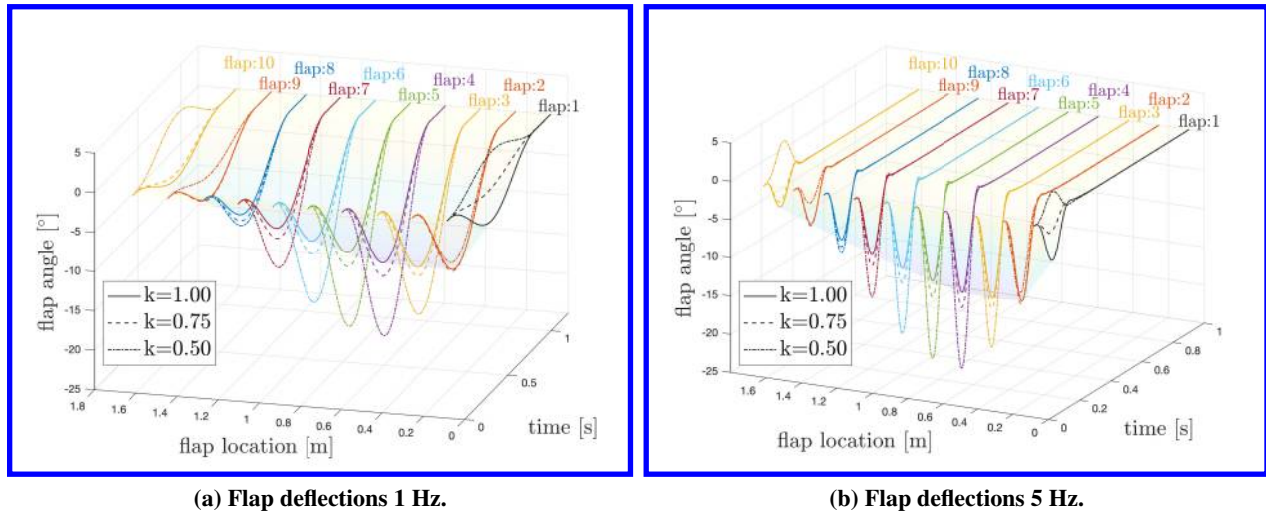


Fig. 15 Spanwise flap deflections comparison for two frequencies and varying scaling parameter.

the GLA controller for gusts of 1 Hz and 5 Hz, was evaluated with the aircraft planform. These allocations are shown in Figures 15a and 15b. The flap deflections at transient peaks (maximum flap deflection) for $k = 0.50$ are shown in Tab. 5. For 1 Hz and 5 Hz, these are at ≈ 0.5 and ≈ 0.125 , respectively.

Table 5 Peak flap deflections ([deg]) for 1 Hz and 5 Hz gust frequencies at $k = 0.50$ and $V_\infty = 35$ m/s.

	β_1	β_2	β_3	β_4	β_5	β_6	β_7	β_8	β_9	β_{10}
1.00 Hz	2.9904	-10.976	-18.144	-21.322	-20.47	-17.76	-13.624	-8.4668	-2.4377	4.5271
5.00 Hz	2.9722	-10.556	-18.451	-21.843	-21.152	-18.448	-14.248	-8.9932	-2.8749	4.1325

The analysis was performed in XFLR5 at $V_\infty = 35$ m/s at cruise conditions. In particular, an initial assessment of the pressure distribution, induced drag, and the wake behavior behind the wing was studied. Figures 16a and 16b show the wake characteristics of the corresponding gust frequencies. Figures 17a and 17b show the pressure distributions of the corresponding frequencies.



Fig. 16 Wake characteristics at $V_\infty = 35$ m/s corresponding to the flap angles in Tab. 5.

As can be seen from Tab. 5 the deflections are comparable but relatively higher for the 5 Hz frequencies. The corresponding lifts distributions observed from the XFLR5 analysis are also sharper. In both cases, a low-pressure region is generated by upward deflections of the inboard flaps, which consequently reduces the lift to counter the incoming gust. Due to more extensive flaps settings, more considerable induced drag (yellow) and wake (purple) are generated behind the wing at 5 Hz. It must be noted that the aerodynamic solution found for these cases is a steady-state solution and does not include the effect of transient allocation. However, these initial analysis results suggested that the allocation cannot be carried out without an additional drag penalty. Therefore, additional analysis is recommended to study the drag penalty associated with the flap deflections and possibly include this as an additional objective for the LQR controller.

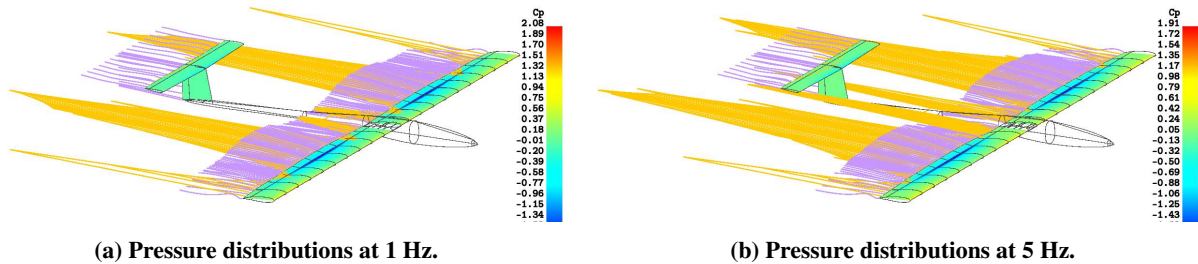


Fig. 17 Pressure distributions and streamlines at $V_\infty = 35$ m/s corresponding to the flap angles in Tab. 5.

VI. Conclusion and Recommendation

A distributed over-actuated aeroelastic wing demonstrator was developed in the scope of the Smart-X project, aiming to demonstrate in-flight performance optimization and multi-objective control with over-actuated wing designs. Aerodynamic and structural analyses were performed to determine actuator torque requirements and actuation mechanism design. The effect of actuator design was studied through a series of gust simulations of closed-loop control of a parametric aeroservoelastic model for gusts with various frequencies. Actuator dynamics were implemented in the system through scaling of the stiffness and damping of a second-order system. With the nominal LQR controller, reductions of peak gust load up to 78 % were achieved compared to the open-loop case. It was observed that lower scaling corresponding to faster actuation provides significant improvements of up to 11 percent over the nominal actuator configuration, yielding reductions of gust loads up to 84 %. Furthermore, it was observed that the effectiveness of faster actuators improves for higher frequency gusts. This confirms the potential of SmartX-Neo to deal with faster control objectives more effectively.

It must be noted that the result presented here consider a purely numerical scenario with full state feedback of the system. In a more realistic case, the noise and bandwidth limitations of the sensors will impact the effectiveness of GLA. It is recommended to include and study these effects in further research. Furthermore, it is recommended to evaluate the prioritization of objectives on the effectiveness of gust load alleviation.

Finally, the manufacturing and integration of the wing demonstrated were discussed preparatory to future static and dynamic wind-tunnel tests at the Open Jet Facility (OJF) wind tunnel.

Acknowledgments

We want to acknowledge Martin Weberschock from Weberschock Development for facilitating the manufacturing of the SmartX-Neo. We would also like to acknowledge his valuable contribution to the manufacturing process and suggested improvements to the design of the wing.

References

- [1] Lentink, D., Müller, U. K., Stamhuis, E. J., De Kat, R., Van Gestel, W., Veldhuis, L. L., Henningsson, P., Hedenström, A., Videler, J. J., and Van Leeuwen, J. L., "How swifts control their glide performance with morphing wings," *Nature*, Vol. 446, No. 7139, 2007, pp. 1082–1085. <https://doi.org/10.1038/nature05733>.
- [2] Bomphrey, R. J., Henningsson, P., and Hedenstro, A., "Efficiency of Lift Production in Flapping and Gliding Flight of Swifts," *PLoS ONE*, Vol. 9, No. 2, 2014. <https://doi.org/10.5061/dryad.cn252>.
- [3] JEX, H., and CULICK, F., "Flight control dynamics of the 1903 Wright Flyer," *12th Atmospheric Flight Mechanics Conference*, American Institute of Aeronautics and Astronautics, Reston, Virginia, 1985, pp. -. <https://doi.org/10.2514/6.1985-1804>, URL <http://arc.aiaa.org/doi/10.2514/6.1985-1804>.
- [4] Mkhoyan, T., Thakrar, N. R., De Breuker, R., and Sodja, J., "Design and Development of a Seamless Smart Morphing Wing Using Distributed Trailing Edge Camber Morphing for Active Control," *AIAA Scitech 2021 Forum*, 2021, p. 0477.
- [5] Mkhoyan, T., Thakrar, N. R., De Breuker, R., and Sodja, J., "Design of a Smart Morphing Wing Using Integrated and Distributed Trailing Edge Camber Morphing," *ASME 2020 Conference on Smart Materials, Adaptive Structures and Intelligent Systems*, American Society of Mechanical Engineers, 2020, pp. -. <https://doi.org/10.1115/smasis2020-2370>, URL <https://asmedigitalcollection.asme.org/SMASIS/proceedings/SMASIS2020/84027/Virtual,Online/1090388>.

- [6] Wang, X., Mkhoyan, T., Mkhoyan, I., and De Breuker, R., “Seamless Active Morphing Wing Simultaneous Gust and Maneuver Load Alleviation,” *Journal of Guidance, Control, and Dynamics*, Vol. 44, No. 9, 2021, pp. 1649–1662. <https://doi.org/10.2514/1.G005870>.
- [7] Werter, N. P., Sodja, J., Spirlet, G., and De Breuker, R., “Design and experiments of a warp induced camber and twist morphing leading and trailing edge device,” *24th AIAA/AHS Adaptive Structures Conference*, 2016. <https://doi.org/10.2514/6.2016-0315>, URL <http://arc.aiaa.org>.
- [8] Deperrois, A., *XFLR5 Theoretical overview*, 2021. URL <http://www.xflr5.tech/xflr5.htm>.
- [9] Systèmes, D., *ABAQUS/CAE Theory Guide, Version 6.19*, Dassault Systèmes, 2019.
- [10] Jongkind, K., Falkmann, A., and van der Veer, H., “Open Jet Facility,” , 2020. URL <https://www.tudelft.nl/lr/organisatie/afdelingen/aerodynamics-wind-energy-flight-performance-and-propulsion/facilities/low-speed-wind-tunnels/open-jet-facility/>.
- [11] Drela, M., *XFOIL: an analysis and design system for low Reynolds number airfoils.*, 54), Berlin, Germany, Springer-Verlag, 1989, Springer-Verlag Wien, 1989.
- [12] Volz, “Volz DA 22 Actuator Technical Specification,” Tech. rep., Volz Servos GmbH, 2013.
- [13] De Breuker, R., Binder, S., and Wildschek, A., “Combined active and passive loads alleviation through aeroelastic tailoring and control surface/control system optimization,” *AIAA Aerospace Sciences Meeting, 2018*, Vol. 1, No. 210059, 2018. <https://doi.org/10.2514/6.2018-0764>, URL <https://arc.aiaa.org/doi/pdf/10.2514/6.2018-0764>.
- [14] Theodorsen, T., “General theory of aerodynamic instability and the mechanism of flutter (NACA-TR-496),” *National Advisory Committee for Aeronautics, Langley Field, VA*, 1949. URL <http://www.tree-o-life.org/ARO202/naca-report-496.pdf>.
- [15] Leishman, J. G., “Subsonic unsteady aerodynamics caused by gusts using the indicial method,” *Journal of Aircraft*, Vol. 33, No. 5, 1996, pp. 869–879. <https://doi.org/10.2514/3.47029>, URL <http://arc.aiaa.org/doi/10.2514/3.47029>.
- [16] Wang, X., Mkhoyan, T., and De Breuker, R., “Nonlinear Incremental Control for Flexible Aircraft Trajectory Tracking and Load Alleviation,” *Journal of Guidance, Control, and Dynamics*, Vol. 1, No. January, 2021, pp. 1–19. <https://doi.org/10.2514/1.G005921>.
- [17] Ferrier, Y., Nguyen, N. T., Ting, E., Chaparro, D., Wang, X., de Visser, C. C., and Chu, Q. P., “Active gust load alleviation of high-aspect ratio flexible wing aircraft,” *2018 AIAA Guidance, Navigation, and Control Conference*, 2018, p. 0620.
- [18] Sika, “Model and Mold Manufacturing,” , 2021. URL <https://industry.sika.com/en/home/advanced-resins/model-and-mold-manufacturing.html>.
- [19] multiSIM, “multiSIM: Distributed simulation D-SIM,” , 2021. URL <https://multisim.nl/d-sim/>.

Appendix A. Planform Parameters

Table 6 Planform parameters.

Item	Symbol	Value	Unit
Wing aspect ratio	\mathcal{R}	13.6	[-]
Wing span	b_w	3.4	[m]
Wing loading	b_w	6.706	[kg/m ²]
Fuselage length	L_f	2.345	[m]
Elevator span	b_e	0.56	[m]
Vertical stabilizer span	b_s	0.25	[m]
Wing chord	(NACA 0015) c_w	0.25	[m]
Elevator chord (root,tip)	(NACA 0010) c_e	(1.67,1.45)	[m]
Vertical stabilizer chord (root,tip)	(NACA 0010) c_s	(0.24,0.19)	[m]
Elevator incidence angle	α_i	-4	[°]
Fuselage position	x (w.r.t. wing) x_f	-0.645	[m]
c.g. position	x (w.r.t. wing) x_{cg}	0.027	[m]
Neutral point	x (w.r.t. wing) x_{np}	0.305	[m]
Total mass	W_t	5.7	[kg]
Payload mass	W_p	1.5	[kg]